2021 17th International Conference on Distributed Computing in Sensor Systems (DCOSS) | 978-1-6654-3929-9/21/$31.00 ©2021 IEEE | DOI: 10.1109/DCOSS52077.2021.00073

Chirp Spread Spectrum Modulation for Intrabody Nanoscale Communication and Sensing

Honey Pandey
Dept. of Electrical Engineering
University at Buffalo
Buffalo, NY, USA
honeypan@buffalo.edu

Josep Miquel Jornet
Dept. of Electrical and Computer Engineering
Northeastern University
Boston, USA
jmjornet@northeastern.edu

***Abstract*—Optical signals are commonly used for intrabody applications, such as nano-bio-sensing and imaging and, more recently, nanoscale communication. However, due to the interaction of light with the building blocks of different body tissues, including different types of cells, organelles, and molecular components, the intrabody channel is highly frequency selective, compromising the communication between intrabody nano-devices as well as wearable devices. In this paper, Chirp Spread Spectrum (CSS) modulation is proposed as a way to overcome the frequency selectivity of the optical channel in intrabody applications. More specifically, after reviewing and highlighting the key properties of the intrabody optical channel, the performance of CSS analytically derived. Extensive numerical results are provided both for a generic optical frequency selective channel and for the near-infrared optical in-vivo channel to illustrate the performance of CSS. The obtained results demonstrate how the possibility to detach the symbol duration from the actual signal bandwidth leads to low bit error rates even when operating in very low signal to noise ratio conditions.**

***Index Terms*—Nanoscale communication, nanonetworks, intrabody optical channel, chirp spread spectrum.**

I. Introduction

In recent years, nanotechnology has enabled the development of miniature devices that can be embedded in the body to observe and even control bodily events at the nanoscale in real-time [1–4]. Among the many different enabling technologies for nano-bio-sensing, one of the key promising approaches relies on the use of surface plasmon resonance (SPR) nanosensors to analyze circulating biomarkers in body fluids for the diagnosis of deadly diseases, ranging from different cardiovascular and neuronal diseases [5–8] to, more recently, different types of cancer directly from blood [9–12]. In SPR-based nano-bio-sensing, an electromagnetic (EM) signal in the near infrared (NIR, 800-2500 nm) or visible (400-800 nm) spectrum is utilized to excite biofunctionalized nanoparticles or nano-patterned microsurfaces, and their sensing-status-dependent response in reflection is measured. While the SPR structures are very small, existing nano-bio-sensing systems require bulky and expensive equipment limiting the practical applications of this technology. Ideally, we would like to miniaturize the equipment and enable in-vivo systems, a direction in which there has been major progress in the recent years, including the development of miniature plasmonic nano-lasers [13], nano-antennas [14] and single photon detectors [15].

In parallel to these developments, major advancements in the fields of electronics, photonics, and wireless communication technologies have enabled the development of compact wearable devices, with applications in diverse fields such as medical, wellness, fitness, security, or even business operation [16], [17]. However, existing wearable devices are only able to measure very few parameters, such as heart rate, breathing, temperature, or blood pressure [18], [19]. At the intersection of the two fields, our team has proposed before a new generation of wearable devices that can serve as the mechanism to replace the external equipment that is needed in nano-bio-sensing systems and, ultimately, to enable a direct interface between nano-bio-events and macro-users [20–22].

When designing communication systems either to enable the communication between intrabody nano-devices or implanted nano-devices and wearable devices, there are two fundamental aspects to take into account. On the one hand, the very small wavelength of optical signals leads to very high spreading losses and, thus, very short communication ranges. On the other hand, from the nanoscale perspective, the human body is not a material with homogeneous permittivity or permeability. Instead, it is a collection of different types of elements, such as cells, organelles, and molecules, with different geometry, arrangement and EM properties. Each element introduces frequency-dependent absorption and scattering, in addition to multi-path propagation [23], [24], resulting in a highly frequency selective channel that introduces several challenges for practical optical nanoscale communication systems.

Existing communication schemes for intrabody optical communication rely on the utilization of very short, femtosecond-long pulses [25] (i.e., up to two orders of magnitude shorter than those utilized for terahertz nanoscale communications [26]). Such pulses have been widely used both for nano-bio sensing (e.g., SPR-based sensing and spectroscopy) and actuation of biological systems (e.g., in optogenetics and optogenomics applications) and can be utilized as the basis of on-off keying modulations. However, the frequency selectivity of the channel results in temporal broadening and distortion of the waveforms and, ultimately, leads to neither efficient nor effective use of the spectrum. While spectral efficiency is generally not a concern in nano-bio applications (the latency at which biological systems operate leads to very low information generation rates), the information reliability is critical.

In this paper, we propose for the first time to utilize chirp spread spectrum (CSS) modulation for intrabody wireless communication and sensing applications. While largely embraced in radar applications due to its multi-resolution sensing capabilities (also at optical frequencies [27]), this modulation scheme has become a popular choice for wireless communications over frequency-selective channels, such as in

978-1-6654-3929-9/21/$31.00 ©2021 IEEE
DOI 10.1109/DCOSS52077.2021.00073

Authorized licensed use limited to: Fondren Library Rice University. Downloaded on January 03,2023 at 14:38:57 UTC from IEEE Xplore. Restrictions apply.

Low Power Wide Area Networks such as LoRaWAN [28] and underwater acoustic networks [29]. Motivated by the intrinsically frequency-selective nature of the optical intra-body mainly due to absorption and scattering phenomena, we suggest the use of CSS to increase the distance over which information can be reliably transmitted. After reviewing the intrabody optical channel, we formally define the key blocks of a CSS-based system and we numerically investigate the impact of different types of frequency selective behaviors on the performance of the system in terms of the achievable data rates and, more importantly, bit error rate (BER). Finally, as a study case, we illustrate the performance of CSS over the intrabody NIR channel between a wearable device and an implanted nano-bio-sensor.

The remainder of the paper is organized as follows. In Sec. II, we review the main properties of the intrabody optical channel and the model to be utilized in our analysis. In Sec. III, we define the system architecture for a CSS-based communication system. In Sec. IV, we provide extensive numerical results for CSS in a generic frequency selective channel as well as in the intrabody NIR channel. Finally, we conclude the paper in Sec. V.

II. Intrabody Optical Channel Model

We consider an application scenario where a wearable device communicates with an implanted nano-bio-sensor. The channel between the two devices is described by the cascaded model [21] shown in Fig. 1. This consists of four different layers, namely, air, skin (epidermis and dermis layers), blood and fat. Here, "Th" refers to the thickness of each layer.

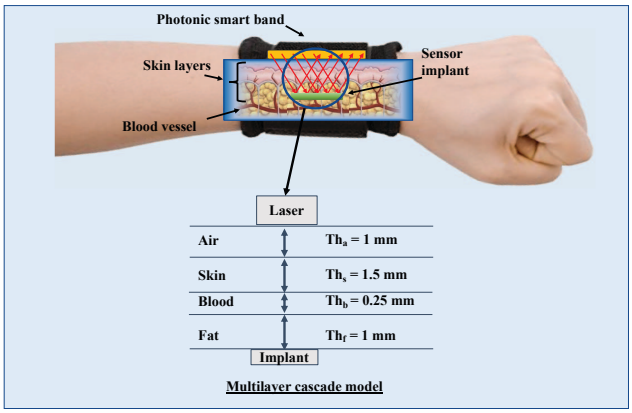

Fig. 1: Multi-layer cascade model of skin tissue for wearable to implant communication.

The propagation of optical signals through the layers depends on the EM properties of each layer:

1) Refractive Index: The propagation of light is determined by the refractive index of the material that the signal will propagate through (in our case, starting by air as shown in Fig. 1. An effective formula to tabulate the refractive index of air (n_{air}) as a function of the wavelength (λ) is [30]:

$$n_{air}(\lambda) = 1 + \frac{0.05792105}{238.0185 - \lambda^{-2}} + \frac{0.00167917}{57.362 - \lambda^{-2}}. \quad (1)$$

The refractive index of the whole skin is given by [31]:

$$n_{skin}(\lambda) = 1.309 - 4.346 \cdot 10^2 \cdot \lambda^{-2} + 1.6065 \cdot 10^9 \cdot \lambda^{-4} - 1.2811 \cdot 10^{14} \cdot \lambda^{-6}. \quad (2)$$

The refractive index of blood and fat can be calculated using the Sellmeier Formula:

$$n^2(\lambda) = 1 + \frac{A_1 \cdot \lambda^2}{\lambda^2 - B_1} + \frac{A_2 \cdot \lambda^2}{\lambda^2 - B_2}, \quad (3)$$

where the values for the empirical constants (A_1, A_2, B_1, B_2) are provided in [32], [33]. The SPR-based nano-bio implant has a coating of gold, whose electronic properties are well-defined [34]. All these equations are utilized to calculate only the real part of the refractive index.

2) Absorption and Scattering Coefficients: The absorption coefficient μ_{abs} determines the amount of light absorbed by the medium (or converted from EM energy into kinetic or thermal energy). Different layers in the cascaded model are integrated by different types of components, but ultimately it all comes down to having different types of molecules and molecular arrangements. Different molecules have different absorption spectra and, moreover, these can quickly change even for small variations of the wavelength [35].

In the NIR spectrum, the main chromophores (molecules responsible for light absorption over a range of wavelengths thus providing the color [36]) of the human skin tissue and subcutaneous fat tissue are water and lipids [37]. The absorption coefficients can be calculated by the following equation [38]:

$$\mu_{abs}(\lambda) = vf_{water} \cdot \mu_{abs}^{water}(\lambda) + vf_{lipid} \cdot \mu_{abs}^{lipid}(\lambda), \quad (4)$$

where vf_{water}, μ_{abs}^{water} and vf_{lipid}, μ_{abs}^{lipid} are the volume fractions and absorption coefficients of water [39] and lipid [40], respectively. The volume fractions for whole skin is 0.7% of water and 0.3% of lipids and for fat tissues it is 0.122% of water and 0.896% of lipids.

In addition to absorption, light suffers from scattering too [41]. The reduced scattering parameter, $\mu_s^{'} = (1-g)\mu_s$, is generally used for light propagation in biological tissues. For biological tissues, the *anisotropy factor*, g is in the range of $0.5 \leq g \leq 0.95$, which indicates that forward scattering is dominant.

The reduced scattering coefficients of skin and fat are given by [37]:

$$\mu_s^{skin}(\lambda) = 73.7 \cdot (\lambda)^{-0.22} + 1.1 \cdot 10^{12} \cdot (\lambda)^{-4}, \quad (5)$$

$$\mu_s^{fat}(\lambda) = 1050.6 \cdot (\lambda)^{-0.68}. \quad (6)$$

To determine the optical properties of the human blood, we first note the composition of the whole blood (red blood cells, white blood cells, platelets and blood plasma). In the wavelength range above 1100 nm, the absorption of blood is mainly dominated by water [42]. Only by removing the water, several absorption features can be identified. One of the main contributor is the red blood cell and its volume fraction, haemoglobin concentration and lastly the oxygen saturation precisely impact the absorption and scattering properties of the blood [43]. For our study, we consider the values of scattering and absorption coefficients for oxygenated whole blood.

Authorized licensed use limited to: Fondren Library Rice University. Downloaded on January 03,2023 at 14:38:57 UTC from IEEE Xplore. Restrictions apply.

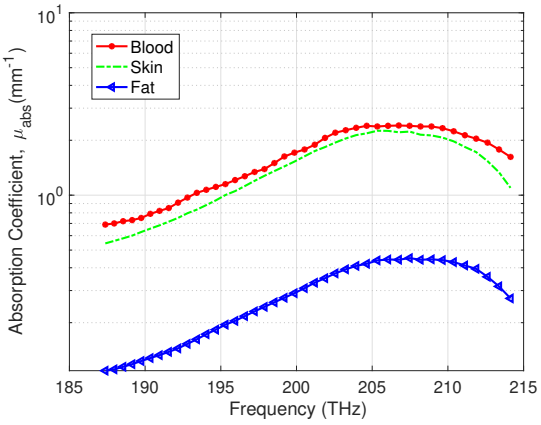

(a) Molecular Absorption Coefficients

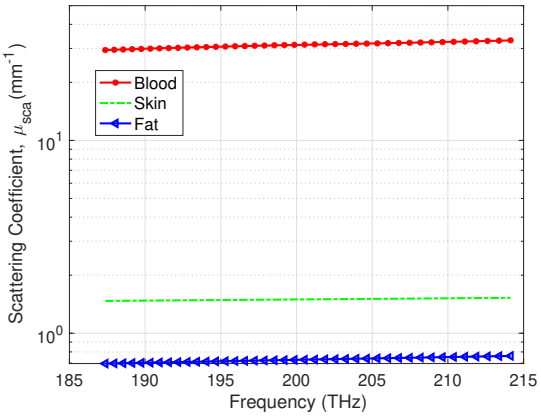

(b) Scattering Coefficients

Fig. 2: Frequency dependency on the absorption and scattering coefficients of the Optical channel.

In Fig. 2, we illustrate the results of the the computed absorption and scattering coefficients of human tissues (fat, skin and blood) at numerous frequencies in the NIR spectrum. Focusing on the absorption coefficients, we notice that the absorption loss for blood is the highest followed by skin and then fat tissue being the least. The same trend applies for the scattering coefficients as well as seen in Fig. 2b. As observed, both absorption and scattering coefficients are around the same value and equally play a significant role in the contribution to pathloss of the optical channel. We can notice that the optical channel model is very lossy and frequency selective.

3) Spreading Loss: While it has been shown before that living cells can act as focusing lenses [24], [44], the spreading of the signal power over large surfaces as it propagates from the emitter (transmitter) to the detector (receiver) leads to very high losses, given by:

$$L_{spr}\left(\lambda, d\right) = -10\log_{10}\left(D\left(\frac{\lambda^2}{4\pi}\right)\left(\frac{1}{4\pi d^2}\right)\right), \quad (7)$$

where d is the distance from the radiation source. This equation has three terms, namely, $\lambda^2/4\pi$ which is the antenna effective aperture; $1/4\pi d^2$ which is the spherical spreading loss; and the antenna directivity gain ($D = 4\pi/\Omega_A$), which is defined as the ratio of the solid angle of a sphere to the radiation solid angle of the antenna, Ω_A. This radiation solid angle depends on the specific radiation pattern of the antenna. For a narrow directional source like a laser with narrow beamwidth $\Delta\theta$ and $\Delta\phi$, Ω_A is given as

$$\Omega_A = \int_{\phi=0}^{\Delta\phi}\int_{\theta=0}^{\Delta\theta} sin\theta d\theta d\phi = \Delta\phi(1 - cos\Delta\theta), \quad (8)$$

where θ and ϕ are the azimuth and polar angles in the spherical coordinate system, respectively [21].

Given the low emission power of the micro/nano-lasers and the high propagation losses, very high sensitivity detectors would be needed to allow communications over meaningful distances. Alternatively, waveforms that can simultaneously overcome the frequency selectivity due to absorption and scattering losses of the channel and operate in low SNR regimes are needed. These are two of the main properties of CSS.

III. Chirp Spread Spectrum System Design

In this section, we describe the transmitter and receiver of a CSS system. While there are different types of chirp waveforms, by keeping under consideration the low computational resources of intra-body nano-devices, we focus on the simplest linear chirp case.

A. Transmitter

In a linear CSS scheme, a logical '1' is transmitted as a linear up-chirp signal and a logical '0' is transmitted as a linear down-chirp s [45]. The linear chirp is a sinusoidal signal whose instantaneous frequency changes linearly with time t for the symbol duration T, between a minimum frequency $f_{min} = f_c - \frac{B}{2}$ and a maximum frequency $f_{max} = f_c + \frac{B}{2}$, where $B = f_{max} - f_{min}$ is the bandwidth and f_c is the carrier frequency of the signal.

The chirp waveform is represented as:

$$s(t) = a(t)cos\theta(t), \quad 0 \leqslant t \leqslant T, \quad (9)$$

where a is the envelope of the chirp signal and θ is the phase of the chirp signal given by:

$$\theta(t) = 2\pi(f_0 t + B\phi(t)) + \theta_0), \quad -\frac{T}{2} \leqslant t \leqslant \frac{T}{2}. \quad (10)$$

ϕ is the integration of the chirp function $\left(\varphi(t) = \frac{t}{T}\right)$ for the linear chirp given by:

$$\phi(t) = \int \frac{t}{T}dt = \frac{t^2}{2T} + c, \quad (11)$$

where c is a constant (integer) value.

Authorized licensed use limited to: Fondren Library Rice University. Downloaded on January 03,2023 at 14:38:57 UTC from IEEE Xplore. Restrictions apply.

From (10) and (11), we obtain the chirp rate $\left(\mu(t) = \frac{B}{T}\right)$ for the linear chirp signal. The up chirp signal and down chirp signal can finally be represented as:

$$s_1(t) = a(t)cos2\pi\left(f_{min}t + \frac{\mu}{2}t^2\right) + \theta_0) \ \ , 0 \leqslant t \leqslant T, \tag{12}$$

$$s_0(t) = a(t)cos2\pi\left(f_{max}t - \frac{\mu}{2}t^2\right) + \theta_0) \ \ , 0 \leqslant t \leqslant T. \tag{13}$$

Fig. 3 shows the chirp signal for a bandwidth of 50 Hz and the time interval of 1 s. Here the frequency sweeps linearly across the pulse-width either in the upward direction (Fig. 3a) or the downward direction (Fig. 3b).

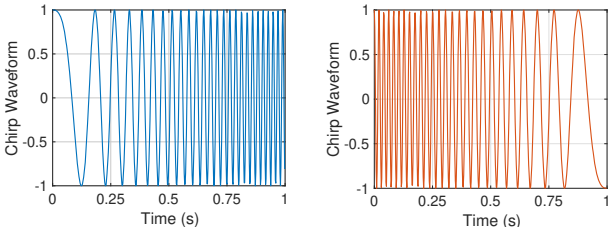

(a) Up-chirp signal (b) Down-chirp signal

Fig. 3: Representation of up-chirp signal and down-chirp signal waveform

B. Receiver

At the receiver, two matched filters, one for the up-chirp and one for the down-chirp, are utilized to demodulate and detect the received bits. In order to maximize the Signal to Noise Ratio (SNR) we utilize the match filter. The impulse response h of an ideal matched filter is the transmitted signal reversed in time and conjugated $\big(h(t) = s^*(\tau - t)\big)$.

We proceed as follows to compute the BER. Under the assumption of symbol time synchronization (for example achieved by utilizing a minimal-length initial synchronization preamble [46]), the received signal $\big(y(t) = s(t) + n(t)\big)$ is multiplied with the up-chirp signal (12) and down-chirp signal (13) respectively to produce the detector outputs:

$$m_i = \int_0^T y(t)s_i(t)dt, \ \ i = 0, 1 \ \ , 0 \leqslant t \leqslant T. \tag{14}$$

Now the data bit is '0' if m_0 is greater than m_1, else it is considered bit '1'. We define the cross-correlation coefficient ρ between down-chirp and up-chirp signals as:

$$\rho = \frac{1}{\sqrt{E_b}}\int_0^T s_0(t)s_1(t)dt, \tag{15}$$

where E_b is the bit energy. Finally, the probability of error at the receiver can be calculated as [47]:

$$P_e = Q\left(\sqrt{\frac{E_b}{2N_0}(1-\rho)}\right), \tag{16}$$

where N_0 is the noise power spectral density (PSD). As a reminder, the relation between the SNR and E_b/N_0 is given by:

$$SNR = \left(\frac{R_b}{B}\right)\left(\frac{E_b}{N_0}\right), \tag{17}$$

where R_b is the bit rate, E_b denotes the bit energy and N_0 states the noise power. In our case, we are considering only binary modulations, therefore, (17) can be rewritten as:

$$\left(\frac{E_b}{N_0}\right) = SNR \cdot B \cdot T_s, \tag{18}$$

where T_s is the symbol duration.

IV. Numerical Performance Analysis of CSS

In this section, the performance of CSS in optical frequency-selective channels is analyzed.

A. System Parameters

Table I summarizes all the parametric values utilized for our CSS system analysis in the different channels including a generic frequency selective optical channel and the NIR channel. As already mentioned before, whereas in a traditional communication system, the symbol duration T_s directly depends on the bandwidth, in a CSS system, we can independently adjust the symbol time and bandwidth.

B. Generic Frequency-selective Optical Channel

For the analysis of the CSS in a generic frequency-selective optical channel, we chose a wider range of frequencies (187.37 THz - 230.7 THz). Consider a chirp signal is transmitted as shown in Fig. 4 (the figure also shows the PSD of the signal). In our analysis, we consider different types of frequency-selective behaviors. First, we study the impact of having a single wide frequency notch. For example, Fig. 5 shows the result of transmitting the original chirp through a

Channel	Wavelength λ (μm)	Lowest Frequency f_{min} (THz)	Highest Frequency f_{max} (THz)	Starting Frequency f_{ini} (THz)	Bandwidth B (THz)	Symbol Duration T_s (ps)	SNR Range SNR (dB)	No. of Symbols N_s	Attenuation Factor AF
Frequency Selective	1.3 to 1.6	187.37	230.7	187.37	43.2	$\frac{50}{B}$	-50 to 10	1000	0
Optical	1.4 to 1.6	187.37	214.13	187.37	26.76	$[0.5, 1, 10, 100]\ \frac{1}{B}$	-50 to 10	1000	0

TABLE I: Parametric values for different channels

Authorized licensed use limited to: Fondren Library Rice University. Downloaded on January 03,2023 at 14:38:57 UTC from IEEE Xplore. Restrictions apply.

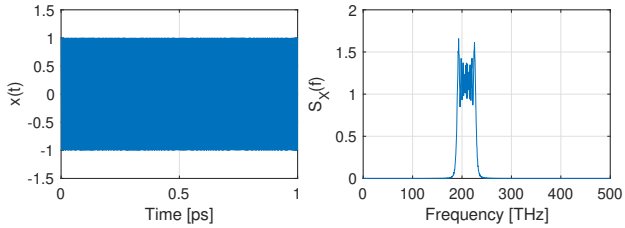

Fig. 4: Initial transmitted signal with no frequency distortion

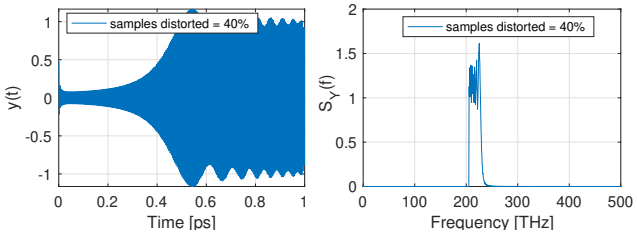

Fig. 5: Continuous distortion of 40% of signal frequencies

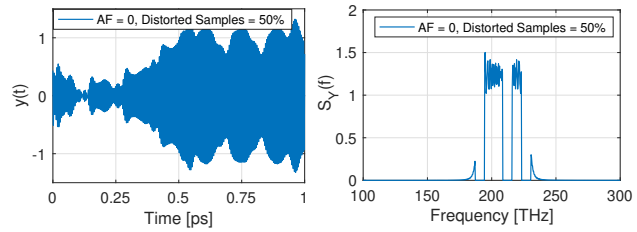

Fig. 6: Notch distortion of 50% of signal frequencies

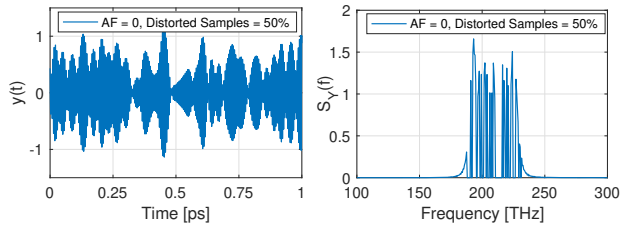

Fig. 7: Random distortion of 50% of the signal frequencies

frequency selective channel where 40% of the signal samples are continuously distorted. Another type of frequency selectivity can come in the form of multiple narrower frequency notches. In Fig. 6, we show an example for a signal whose PSD has had the beginning, mid and ending fully attenuated (wiped out) 50% of the original signal. In an extreme case, in Fig. 7, we illustrate the case in which 50% randomly-selected frequencies of the signal are totally eliminated.

Fig. 8 shows the BER as a function of SNR for different signal distortion values for the different types of generic frequency selective channel. In these results, the chirp signal is analyzed for a symbol duration $T_s = 50/B$ and the SNR range of -50 dB to 10 dB. While this SNR range might seem very low, the high $B \cdot T_s$ product leads to high E_b/N_0 ratio. Fig. 8a illustrates the behavior starting from the beginning of the signal. We notice that even when 95% of the signal is distorted, the BER can be significantly low even if the SNR is still at -5 dB. When no samples are distorted, for a SNR of -25 dB, the BER is still noticeably low. This shows that, no matter what percentage of the signal is destroyed, as long as there is a part of the signal retained, the transmitted bit data can be regained. This shows the performance of the CSS scheme with a frequency selective channel. Further, we will explore non-continuous signal distortions (notch distortion and random distortion) to analyze the CSS performance.

In Fig. 8b, different proportions of the signal are distorted and the BER with respect to SNR is inspected. We notice that when close to 95% of signal is impacted, the required SNR to achieve reasonably low BER is close to 10 dB less than when the signal frequencies are continuously removed from the beginning of the signal to almost 95% of Fig. 8a. In case of the former graph, we definitely retain signal samples from the middle section of the signal, whereas, in the latter case, the samples that remain are only in the end of the received signal. Therefore, it is more difficult to identify the bit that was transmitted initially.

In Fig. 8c, we show the BER as a function of the SNR for different distortion percentages of the signal being randomly attenuated. Since the cancelled frequencies are randomly selected, we notice slightly better performance, as the signals are not distorted from the starting position, so we get data points from different parts of the signals which makes the rate of signal detection slightly higher in comparison to the earlier case of signal being tampered from the beginning (Fig. 8a). Lastly, in Fig. 8b, we can see the minimum required SNR for 95% of samples distortion at $AF = 0$ lies between -15 dB to -5 dB as the received samples after impairment can belong either to the beginning, middle or end of the original signal. This type of distortion shows close to 5 dB better performance in contrast to random distortion.

C. NIR Channel between a Wearable Device and an Implanted Nano-bio-sensor

Now that we have seen the functionality of CSS in a generic frequency selective optical channel, we study the specific NIR channel. Here a bit represents one signal instantiate sent by a wearable laser/excitation system and reflected at the implant. To realize the strength of the system we transmit multiple bits and compute the rate at which they are successfully received. Each time the signal is sent to the implant and reflected back from it, it is represented by a bit. The BER as a function of the SNR for chirp modulation numerically analyzed at optical frequencies for intrabody communications system is seen in Fig. 9. Different symbol times are considered. As mentioned before, the low power of compact lasing systems and the high losses requires the utilization of long transmission times to increase the bit energy.

In comparison to Binary Phase Shift Keying (BPSK) modulation, we notice that chirp modulation has a better performance by providing the target BER with the lowest SNR at optical frequencies. Consider $T_s = 1/B$ which is the same symbol duration considered as default for BPSK. There is close to 10 dB improvement when using the CSS modulation method. Few points to be noted in case of CSS are: a) For the same SNR, the BER achieved by CSS is better but the BER is independent of SNR instead depends on Eb/No, so if we were to convert SNR using (18), we can see the dependence as Eb/No is directly proportional to symbol duration T_s. b) To achieve larger Eb/No would mean larger symbol time leading

Authorized licensed use limited to: Fondren Library Rice University. Downloaded on January 03,2023 at 14:38:57 UTC from IEEE Xplore. Restrictions apply.

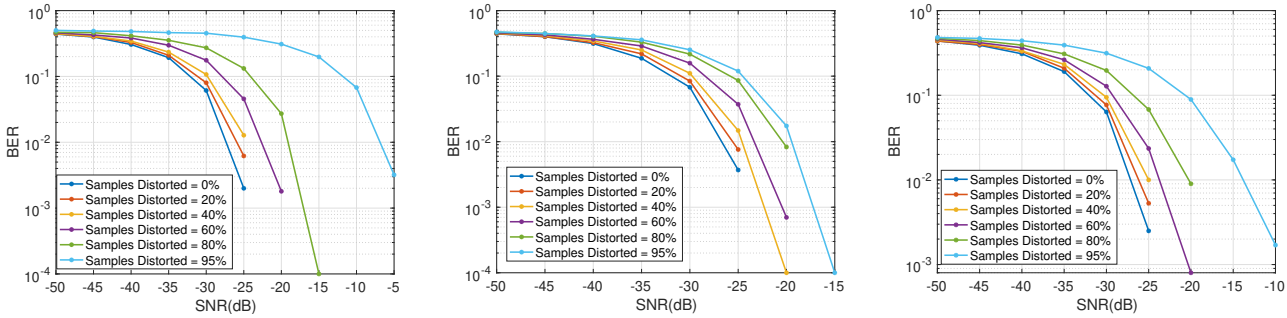

(a) Continuous distortion (b) Notch distortion (c) Random distortion

Fig. 8: The SNR vs BER of generic frequency selective channels

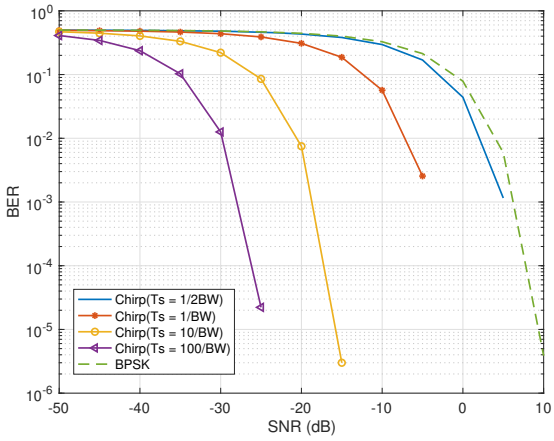

Fig. 9: Chirp Modulation at Optical Frequencies

to slower communication rate, in case of the application of intrabody this factor does not play a significant role as we do not require very large data rates. Instead we focus more on how the signal can cover the entire frequency band or how reliable is the signal over the frequency band. However, we are keen on communicating over the large bandwidth as a portion of the information maybe in the frequency and be a part of the bandwidth itself. We know that by spreading with chirp we are transmitting less information per second and, thus, effectively utilizing the bandwidth less. Ultimately, we are trading bit-rate for robustness to frequency selectivity. Moreover, in the context of sensing, a chirp signal allows multi-frequency/multi-wavelength resolution, which can be beneficial in future joint communication and sensing applications.

V. Conclusion

In this paper, we have provided an in depth study of CSS for intrabody applications. Chirps were initially known to have applications in radar and sonar but have recently extended their use to IoT, even underwater. Chirp modulations have been used in communications mainly for the robustness against channel frequency selectivity such as those resulting from multi-path propagation in traditional wireless networks, but also those created by molecular absorption, for example, over the air at terahertz-band frequencies [48]. Here, after reviewing the properties of the optical wireless intra-body channel, we have illustrated the impact of frequency selectivity for a generic optical channel by inducing three types of distortions comprising of *i*) continuous distortion, *ii*) notch distortion and *iii*) random distortion. We have shown that as long as not all the signal in the entire frequency band is damaged at the same time, a well designed receiver can recover a heavily frequency-selective signal even in the presence of high noise. Further, we have tested CSS over the NIR channel. Ultimately, the possibility of independently controlling the symbol length and the signal bandwidth makes the use of CSS very suitable for intrabody systems, where data-rates might be crucial, but operating over very low SNR margins is needed. As part of our future work, we will explore the use of CSS for joint simultaneous communications and sensing, we will study of the photothermal effects, and we will consider the possibility of utilizing a similar framework for intrabody terahertz-band communications. Moreover, we will consider the Doppler effect resulting from mobility of intrabody devices.

Acknowledgment

This work was supported by the U.S. National Science Foundation (NSF) Awards Number IIP-1718177, CBET-1706050 and CBET-2039189.

References

[1] S. Carrara, "Technologies for an implantable nano-bio-sensing laboratory," *Sensors*, vol. 12, pp. 6520–6537, 2012.
[2] C. Liu, X. Zeng, Z. An, Y. Yang, M. Eisenbaum, X. Gu, J. M. Jornet, G. K. Dy, M. E. Reid, Q. Gan *et al.*, "Sensitive detection of exosomal proteins via a compact surface plasmon resonance biosensor for cancer diagnosis," *ACS sensors*, vol. 3, no. 8, pp. 1471–1479, 2018.
[3] D. Yu, H. Lee, J. Hong, H. Jung, Y. Jo, B.-H. Oh, B. O. Park, and W. Do Heo, "Optogenetic activation of intracellular antibodies for direct modulation of endogenous proteins," *Nature methods*, vol. 16, no. 11, pp. 1095–1100, 2019.
[4] J. M. Jornet, Y. Bae, C. R. Handelmann, B. Decker, A. Balcerak, A. Sangwan, P. Miao, A. Desai, L. Feng, E. K. Stachowiak *et al.*, "Optogenomic interfaces: Bridging biological networks with the electronic digital world," *Proceedings of the IEEE*, vol. 107, no. 7, pp. 1387–1401, 2019.
[5] C. L. Wong and M. Olivo, "Surface plasmon resonance imaging sensors: a review," *Plasmonics*, vol. 9, no. 4, pp. 809–824, 2014.
[6] H. H. Nguyen, J. Park, S. Kang, and M. Kim, "Surface plasmon resonance: a versatile technique for biosensor applications," *Sensors*, vol. 15, no. 5, pp. 10 481–10 510, 2015.
[7] A. Qureshi, Y. Gurbuz, and J. H. Niazi, "Biosensors for cardiac biomarkers detection: A review," *Sensors and Actuators B: Chemical*, vol. 171, pp. 62–76, 2012.

Authorized licensed use limited to: Fondren Library Rice University. Downloaded on January 03,2023 at 14:38:57 UTC from IEEE Xplore. Restrictions apply.

[8] M. Yang, X. Yi, J. Wang, and F. Zhou, "Electroanalytical and surface plasmon resonance sensors for detection of breast cancer and alzheimer's disease biomarkers in cells and body fluids," *Analyst*, vol. 139, no. 8, pp. 1814–1825, 2014.

[9] M. Vendrell, K. K. Maiti, K. Dhaliwal, and Y.-T. Chang, "Surface-enhanced raman scattering in cancer detection and imaging," *Trends in biotechnology*, vol. 31, no. 4, pp. 249–257, 2013.

[10] S. D. Hudson and G. Chumanov, "Bioanalytical applications of sers (surface-enhanced raman spectroscopy)," *Analytical and bioanalytical chemistry*, vol. 394, no. 3, pp. 679–686, 2009.

[11] L. Wu and X. Qu, "Cancer biomarker detection: recent achievements and challenges," *Chemical Society Reviews*, vol. 44, no. 10, pp. 2963–2997, 2015.

[12] P. H. Aoki, L. N. Furini, P. Alessio, A. E. Aliaga, and C. J. Constantino, "Surface-enhanced raman scattering (sers) applied to cancer diagnosis and detection of pesticides, explosives, and drugs," *Reviews in Analytical Chemistry*, vol. 32, no. 1, pp. 55–76, 2013.

[13] H. Zhao, P. Miao, M. H. Teimourpour, S. Malzard, R. El-Ganainy, H. Schomerus, and L. Feng, "Topological hybrid silicon microlasers," *Nature communications*, vol. 9, no. 1, pp. 1–6, 2018.

[14] M. Nafari and J. M. Jornet, "Modeling and performance analysis of metallic plasmonic nano-antennas for wireless optical communication in nanonetworks," *IEEE Access*, 2017.

[15] D.-D. Wang, C.-W. Ge, G.-A. Wu, Z.-P. Li, J.-Z. Wang, T.-F. Zhang, Y.-Q. Yu, and L.-B. Luo, "A sensitive red light nano-photodetector propelled by plasmonic copper nanoparticles," *Journal of Materials Chemistry C*, vol. 5, no. 6, pp. 1328–1335, 2017.

[16] I. D. C. (IDC), "Worldwide quarterly wearable device tracker," *[Online]. Available: https://www.idc.com/getdoc.jsp?containerId=prUS45737919, Accessed on: December 2019*. [Online]. Available: https://www.idc.com/getdoc.jsp?containerId=prUS45737919

[17] Statista, "Use of wearable devices: Which type of wearable device interests you most?" *[Online]. Available: https://www.statista.com/forecasts/790472/interest-in-wearable-devices-in-the-us, Accessed on: December 2019*. [Online]. Available: https://www.statista.com/forecasts/790472/interest-in-wearable-devices-in-the-us

[18] S. Movassaghi, M. Abolhasan, J. Lipman, D. Smith, and A. Jamalipour, "Wireless body area networks: A survey," *IEEE Communications Surveys & Tutorials*, vol. 16, no. 3, pp. 1658–1686, 2014.

[19] S. Seneviratne, Y. Hu, T. Nguyen, G. Lan, S. Khalifa, K. Thilakarathna, M. Hassan, and A. Seneviratne, "A survey of wearable devices and challenges," *IEEE Communications Surveys & Tutorials*, vol. 19, no. 4, pp. 2573–2620, 2017.

[20] H. Guo, J. M. Jornet, Q. Gan, and Z. Sun, "Cooperative raman spectroscopy for real-time in vivo nano-biosensing," *IEEE transactions on nanobioscience*, vol. 16, no. 7, pp. 571–584, 2017.

[21] P. Johari, H. Pandey, and J. M. Jornet, "Interconnecting wearable devices with nano-biosensing implants through optical wireless communications," in *Optical Diagnostics and Sensing XVIII: Toward Point-of-Care Diagnostics*, vol. 10501. International Society for Optics and Photonics, 2018, p. 105011C.

[22] A. Sangwan, H. Pandey, P. Johari, and J. M. Jornet, "Increasing the communication distance between nano-biosensing implants and wearable devices," in *2018 IEEE 19th International Workshop on Signal Processing Advances in Wireless Communications (SPAWC)*. IEEE, 2018, pp. 1–5.

[23] H. Guo, P. Johari, J. M. Jornet, and Z. Sun, "Intra-body optical channel modeling for in vivo wireless nanosensor networks," *IEEE transactions on nanobioscience*, vol. 15, no. 1, pp. 41–52, 2015.

[24] P. Johari and J. M. Jornet, "Nanoscale optical wireless channel model for intra-body communications: Geometrical, time, and frequency domain analyses," *IEEE Transactions on Communications*, vol. 66, no. 4, pp. 1579–1593, 2017.

[25] S. Wirdatmadja, P. Johari, A. Desai, Y. Bae, E. K. Stachowiak, M. K. Stachowiak, J. M. Jornet, and S. Balasubramaniam, "Analysis of light propagation on physiological properties of neurons for nanoscale optogenetics," *IEEE Transactions on Neural Systems and Rehabilitation Engineering*, vol. 27, no. 2, pp. 108–117, 2019.

[26] J. M. Jornet and I. F. Akyildiz, "Femtosecond-long pulse-based modulation for terahertz band communication in nanonetworks," *IEEE Transactions on Communications*, vol. 62, no. 5, pp. 1742–1754, 2014.

[27] W. Zou, H. Zhang, X. Long, S. Zhang, Y. Cui, and J. Chen, "All-optical central-frequency-programmable and bandwidth-tailorable radar," *Scientific reports*, vol. 6, no. 1, pp. 1–8, 2016.

[28] F. Adelantado, X. Vilajosana, P. Tuset-Peiro, B. Martinez, J. Melia-Segui, and T. Watteyne, "Understanding the limits of lorawan," *IEEE Communications magazine*, vol. 55, no. 9, pp. 34–40, 2017.

[29] S.-W. Huang, G. Sklivanitis, D. A. Pados, and S. N. Batalama, "Underwater acoustic communications using quasi-orthogonal chirps," in *2017 51st Asilomar Conference on Signals, Systems, and Computers*. IEEE, 2017, pp. 1749–1753.

[30] P. E. Ciddor, "Refractive index of air: new equations for the visible and near infrared," *Applied optics*, vol. 35, no. 9, pp. 1566–1573, 1996.

[31] A. N. Bashkatov, E. A. Genina, and V. V. Tuchin, "Optical properties of skin, subcutaneous, and muscle tissues: a review," *Journal of Innovative Optical Health Sciences*, vol. 4, no. 01, pp. 9–38, 2011.

[32] E. N. Lazareva and V. V. Tuchin, "Blood refractive index modelling in the visible and near infrared spectral regions," *Journal of Biomedical Photonics & Engineering*, vol. 4, no. 1, 2018.

[33] I. Y. Yanina, E. N. Lazareva, and V. V. Tuchin, "Refractive index of adipose tissue and lipid droplet measured in wide spectral and temperature ranges," *Applied optics*, vol. 57, no. 17, pp. 4839–4848, 2018.

[34] D. I. Yakubovsky, A. V. Arsenin, Y. V. Stebunov, D. Y. Fedyanin, and V. S. Volkov, "Optical constants and structural properties of thin gold films," *Optics express*, vol. 25, no. 21, pp. 25 574–25 587, 2017.

[35] F. Martelli, S. Del Bianco, and A. Ismaelli, "Light propagation through biological tissue and other diffusive media: theory, solutions, and software." Society of Photo-Optical Instrumentation Engineers, 2009.

[36] X.-Q. Xu, Y. He, and Y. Wang, "Near-infrared organic chromophores with ph-sensitive, non-radiative emission for intelligent disease treatment," *Cell Reports Physical Science*, p. 100433, 2021.

[37] A. Bashkatov, E. Genina, V. Kochubey, and V. Tuchin, "Optical properties of human skin, subcutaneous and mucous tissues in the wavelength range from 400 to 2000 nm," *Journal of Physics D: Applied Physics*, vol. 38, no. 15, p. 2543, 2005.

[38] R. Nachabe, B. H. Hendriks, A. E. Desjardins, M. van der Voort, M. B. van der Mark, and H. J. Sterenborg, "Estimation of lipid and water concentrations in scattering media with diffuse optical spectroscopy from 900 to 1600 nm," *Journal of biomedical optics*, vol. 15, no. 3, p. 037015, 2010.

[39] K. Wang, W. Wen, Y. Wang, K. Wang, J. He, J. Wang, P. Zhai, Y. Yang, and P. Qiu, "Order-of-magnitude multiphoton signal enhancement based on characterization of absorption spectra of immersion oils at the 1700-nm window," *Optics express*, vol. 25, no. 6, pp. 5909–5916, 2017.

[40] G. B. Altshuler, R. R. Anderson, and D. Manstein, "Method and apparatus for the selective targeting of lipid-rich tissues," Aug. 12 2003, uS Patent 6,605,080. [Online]. Available: http://www.comsol.com/products/multiphysics/

[41] A. D. Klose and E. W. Larsen, "Light transport in biological tissue based on the simplified spherical harmonics equations," *Journal of Computational Physics*, vol. 220, no. 1, pp. 441–470, 2006.

[42] S. L. Jacques, "Optical properties of biological tissues: a review," *Physics in medicine and biology*, vol. 58, no. 11, p. R37, 2013.

[43] N. Bosschaart, G. J. Edelman, M. C. Aalders, T. G. van Leeuwen, and D. J. Faber, "A literature review and novel theoretical approach on the optical properties of whole blood," *Lasers in medical science*, vol. 29, no. 2, pp. 453–479, 2014.

[44] L. Miccio, P. Memmolo, F. Merola, P. Netti, and P. Ferraro, "Red blood cell as an adaptive optofluidic microlens," *Nature communications*, vol. 6, no. 1, pp. 1–7, 2015.

[45] X. Wang, M. Fei, and X. Li, "Performance of chirp spread spectrum in wireless communication systems," in *2008 11th IEEE Singapore International Conference on Communication Systems*. IEEE, 2008, pp. 466–469.

[46] G. N. Karystinos and D. A. Pados, "New bounds on the total squared correlation and optimum design of ds-cdma binary signature sets," *IEEE Transactions on Communications*, vol. 51, no. 1, pp. 48–51, 2003.

[47] S.-W. Huang, "Multicarrier chirp-division multiplexing for rf and underwater acoustic communications," Ph.D. dissertation, State University of New York at Buffalo, 2018.

[48] P. Sen, H. Pandey, and J. M. Jornet, "Ultra-broadband chirp spread spectrum communication in the terahertz band," in *Next-Generation Spectroscopic Technologies XIII*, vol. 11390. International Society for Optics and Photonics, 2020, p. 113900G.

Authorized licensed use limited to: Fondren Library Rice University. Downloaded on January 03,2023 at 14:38:57 UTC from IEEE Xplore. Restrictions apply.